Design and characterization of a monolithic CMOS-MEMS mutually injection-locked oscillator for differential resonant sensing

Pierre Prache, Jérome Juillard, Pietro Maris Ferreira, Nuria Barniol, Marti Riverola

Design and characterization of a monolithic CMOS-MEMS mutually injection-locked oscillator architecture for differential resonant sensing

Pierre Prache[1,2], Jérôme Juillard[1], Pietro Maris Ferreira[1], Nuria Barniol[2], Marti Riverola[2]

***Abstract*—In this paper we build a proof of concept of a differential sensor based on the phase-difference of two injection-locked MEMS resonators, strongly coupled by a digital mixer. We prove for the first time the feasibility of a fully monolithically co-integrated CMOS-MEMS differential resonant sensor, exploiting the capabilities of the injection-locked synchronization. We present the advantages of such an architecture in term of sensitivity and drift rejection, as well as its limits (e.g. the reduced locking range). The experimental results highlight the critical points of the architecture's design, on which the emphasis of this article is placed. These results are then compared to the theoretical predictions, showing good agreement.**

***Index Terms*—Microelectromechanical systems; CMOS-MEMS; injection-locked oscillators; analog/digital design, differential sensing; drift rejection; phase noise.**

I. INTRODUCTION

MEMS resonant sensors [1] exploit the sensitivity of the natural frequency of a micromechanical structure to the physical quantity to be sensed (the measurand). As in every sensor, the sensitivity to the measurand must be maximized, and the sensitivity to every other external parameter (noises and drifts) minimized or compensated. Although MEMS resonators have several features making them attractive for resonant sensing applications (reduced size, large quality factor Q [2]), their sensitivity to temperature, through thermal softening and thermal expansion, is an issue, leading to natural frequency shifts that are not related to the physical quantity to be measured. Natural frequency drift of MEMS resonators may be compensated through several techniques.

First, temperature can be sensed with a thermometer, and either correct the natural frequency corrected in a microprocessor, or control a micro-oven in which the resonator is embedded. But embedding a thermometer is a challenge, and the resolution CMOS-compatible devices, between 20mK and 1K [3] is not enough to match the industry's requirements in term of frequency stability. Using a second resonator as temperature sensor can be achieved to correct the frequency information as in the Elite DualMEMS architecture from SiTime [4] or control a micro-oven in [5]. But it comes at the cost of complexity in the case of correction and electrical consumption in the case of micro-ovening. One could think of using the two resonators to simultaneously sense the temperature and the measurand.

The most straightforward approach is to design two nominally-identical resonators with similar natural frequencies, the same thermal drift, but different sensitivities to the measurand, e.g. one resonator undergoes compressive axial stress when an acceleration is sensed, whereas the other is subject to (opposite) tensile axial stress. Each resonator is placed in a separate oscillation loop: the difference of the individual oscillation frequencies is then theoretically drift-free. This approach has been successfully implemented in [6] for temperature compensation in accelerometer. However, drift is properly eliminated only if the two resonators are at the same temperature: thus, they must be as close to each other as possible. The main design challenge of this approach is then to have two separate oscillation loops in close proximity to each other, and to avoid detrimental phenomena caused by parasitic (electrical or mechanical) coupling [8]: in fact, coupling may induce frequency-locking of the oscillator loops, which would result in a dead zone in the sensor response. This issue may be circumvented by using resonators with very different natural frequencies [9] or dual-mode architectures [10] but this comes at the cost of added system complexity and more calibration steps.

Two alternatives to the previous approach have recently emerged. The first one relies on mode-localization phenomena in coupled resonators [11]: it is extensively reviewed in [12]. In this approach, two (or more) nominally-identical resonators are voluntarily coupled through a mechanical [13] or electrostatic [11], [14] restoring force, that is small compared to the intrinsic restoring force of each resonator. This passive coupling scheme leads to energy transfer between them, and to a mode-localization phenomenon that can be used for sensing. For example, the ratio of the modal amplitudes of two weakly-coupled resonators provides a highly sensitive measurement of the natural frequency mismatch of the resonators [15], which was theoretically and experimentally proved to be drift-free [16]. The sensitivity of this technique is theoretically (limited

to) Q times that of a conventional resonant sensor, yet it can be shown that this larger sensitivity entails no resolution enhancement [17]. Although this approach is drift-free, and takes advantage of couplings rather than being hindered by them, it has a few limitations. First of all, it relies on amplitude measurements and therefore requires high resolution analog-to-digital converters (although other output metrics than amplitude ratios may be used [15]). Furthermore, as considered in [16], it is an open-loop technique that requires that an external excitation signal be swept over a frequency band of interest, with unavoidable penalties in terms of response time. However, research is being conducted to make this technique closed-loop [18], [19].

The other emerging alternative is to synchronize two oscillator loops through active coupling and exploit the properties of such systems to perform drift-free sensing. This approach was studied for its benefits in term of phase noise reduction for clocking applications [19], or bias cancellation for gyroscopes [20]. In this approach, as proposed in [20] and extensively studied in [21], one couples the resonators through their actuation voltage, so that they are in a state of mutual injection. Provided their natural frequencies are well-matched, the two-resonator system synchronizes and becomes phase-locked. As shown in [22], the phase difference between the motional or actuation signals is a highly-sensitive, drift-free measurement of the natural frequency mismatch between the resonators. The theoretical framework of the synchronization of resonators by mutual injection-locking is developed in [21]. Compared to the mode-localized approach, the mutually injection-locked oscillator (MILO) approach has a theoretically higher sensitivity at the cost of a reduced dynamic range. The resolution of the two approaches is comparable, but the MILO-based approach is intrinsically closed-loop and, consequently, has a faster response time; furthermore, its output metric, a phase difference, is "quasi-digital". Hence, we think it is better-suited to a VLSI implementation. A first experimental proof of the drift rejection by a MILO-based sensor is given in [22], showing a good agreement with the theory but limitations due to the fact that both CMOS-MEMS resonators are not on the same chip, and do not endure the same thermal drift. The design of fully co-integrated MILO architecture is outlined in [23], and some simulation results are given.

In the present work, we give guidelines for the VLSI-compatible design of a fully monolithic co-integrated CMOS-MEMS MILO. Our own design and experimental results are described and commented. The outline of the paper is as follows: in section II, the properties of MILO architectures are described from a system-level perspective, along with the design constraints they entail. In section III, we explain how these constraints can be met through careful chip design, and co-integration of the CMOS-MEMS MILO. In section IV our experimental results are presented, and compared to the theoretical predictions. Section V contains some concluding remarks and perspectives.

II. Design constraints of MILOs

Injection-locking is one way of synchronizing an oscillator to an external frequency reference: a signal from the frequency reference is "injected" into the oscillator, whose frequency may be pulled-in and locked to that of the reference, as first extensively studied by Adler in [24]. In [25], Mirzaei et al. generalized Adler's theoretical results to the case when two LC-tank oscillators are in mutual injection, i.e. each oscillator is the other's frequency reference, with the purpose of generating two stable signals, with a given $\pi/2$ phase difference. It was pointed out that a key issue in the studied architectures was the intrinsic natural frequency mismatch of the LC-tank resonators, due to the fabrication process, resulting in a phase-difference error proportional to (i) the natural frequency mismatch, and (ii) the quality factor Q of the resonators. As proposed in [20], these seeming disadvantages can be turned into assets in the context of a resonant sensing application: a MILO's phase difference "error" (its shift away from a nominal value, e.g. $\pi/2$) can be used as a highly sensitive, intrinsically differential measurement of the natural frequency mismatch of the resonators. The sensitivity of a MILO phase-difference-based sensor is in fact on the order of Q times that of a "conventional" (single oscillator, frequency-based) resonant sensor. However, this enhancement usually comes at the cost of a reduced operating range [26], and entails no particular advantage in terms of resolution [21], so that the main asset of MILO-based sensors is their capability of delivering differential measurements.

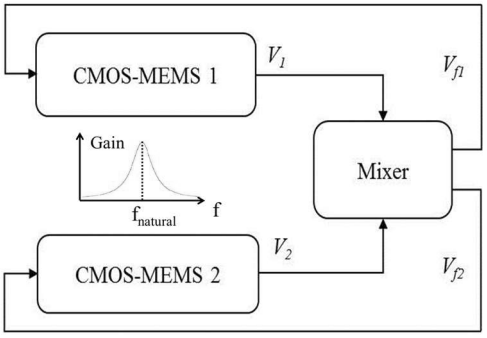

Figure 1: CMOS-MEMS MILO high level schematic.

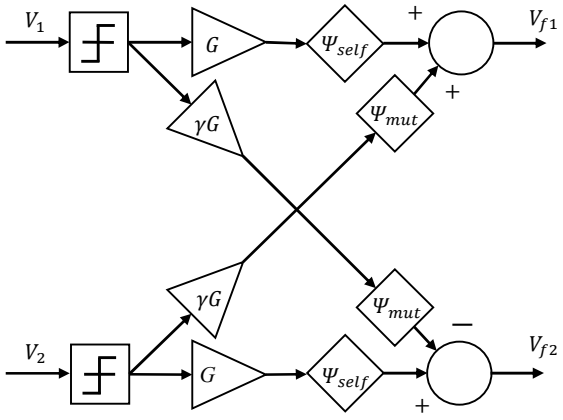

Figure 2: High level nonlinear mixing scheme.

A functional representation of a MILO is shown in Figure 1 it consists in two nominally-identical MEMS resonators with their electronic readouts, coupled through an electronic mixer. The purpose of the mixer is to maintain the two resonators in a phase-locked oscillation state. This may for instance be achieved through linear coupling [27], [28] of two oscillator loops, although this approach requires a good control of the amplitudes of the resonators. In [21], we propose a nonlinear mixing scheme, a simplified version of which is shown in Figure 2 where the coupling signals are issued by the same comparators providing the gain in each oscillation loop.

The coupling gain γ represents the relative amplitude of the mutual-injection signal to the self-injection signal. The phase-shifting elements are chosen so that (i) each resonator is driven at resonance (ii) the nominal phase difference (in the absence of mismatch) between the two resonators is $\phi_0 = \pi/2$. This is done as follows: suppose that resonance is characterized by a certain value of the phase θ_{res} between the output of the readout (V_i), and the mixer output (V_{fi}), e.g. $\theta_{res} = \pi/2$. Then, a few geometrical considerations show that the mutual-injection and self-injection angles must be chosen to satisfy:

$$\begin{aligned}&\sin\left(\theta_{res}+\psi_{self}\right)+\gamma\sin\left(\theta_{res}+\psi_{mut}-\phi_0\right)\\&=\sin\left(\theta_{res}+\psi_{self}\right)-\gamma\sin\left(\theta_{res}+\psi_{mut}+\phi_0\right)=0\end{aligned}, \quad (1)$$

for the MILO to verify the Barkhausen phase criterion at resonance. With a nominal phase difference $\phi_0 = \pi/2$, this boils down to a single equation:

$$\sin\left(\theta_{res}+\psi_{self}\right)-\gamma\cos\left(\theta_{res}+\psi_{mut}\right)=0. \quad (2)$$

A possible choice, done in [25] is to choose the two angles so that both terms on the left-hand side vanish independently of the cross-coupling coefficient:

$$\psi_{self} = -\theta_{res} = \psi_{mut} - \pi/2. \quad (3)$$

Alternatively, one may choose to impose:

$$\psi_{self} = \psi_{mut}, \quad (4)$$

in which case (2) boils down to:

$$\psi_{self} = -\theta_{res} + \operatorname{atan}(\gamma). \quad (5)$$

In the case when $\gamma = 1$, which is of practical importance, this further reduces to:

$$\psi_{self} = -\theta_{res} + \pi/4. \quad (6)$$

From a practical point of view, the second choice (4) – which is the option studied in this paper – requires the implementation of a single electronic block providing the necessary phase-delay (5), whereas the first choice requires an additional block, in order to implement ψ_{mut} with a particular phase relationship with respect to ψ_{self} (3). Furthermore, when the cross-coupling coefficient γ is chosen equal to 1, the implementation of the corresponding mixer with digital electronic blocks becomes straightforward [****], as illustrated in Figure 3.

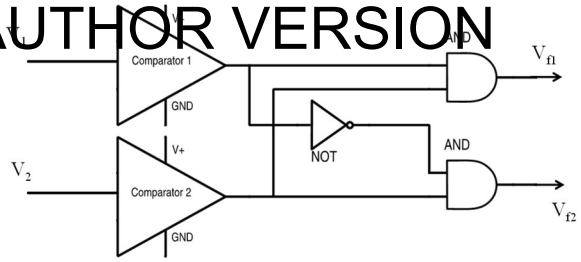

Figure 3: possible implementation of the mixer to match the phase and gain requirements of (6)

Letting ε be the relative stiffness mismatch between the two resonators, a MILO satisfying (4) and (6) has the following characteristics:

$$\left.\frac{\partial\phi}{\partial\varepsilon}\right|_{\varepsilon=0} = Q\times\varepsilon, \quad (7)$$

$$\frac{1}{\omega_0}\left.\frac{\partial\omega}{\partial\varepsilon}\right|_{\varepsilon=0} = \frac{\varepsilon}{4}, \quad (8)$$

$$\varepsilon_{lock} = \frac{\sqrt{2}}{Q}, \quad (9)$$

Where ω_0 is the nominal value of the natural pulsation of the resonators, and ε_{lock} is the locking range of the MILO. Equation (7) corresponds to the sensitivity of the phase-difference (expressed in radians) to stiffness mismatch close to nominal conditions ($\varepsilon = 0$). Relations (7) and (8) are approximately valid across the whole locking range (i.e. provided $|\varepsilon| \le \varepsilon_{lock}$), as illustrated in section IV.C. Beyond the locking range, the oscillation is not stable, so that our second design constraint, besides (6), is that one must be able to fabricate and/or fine tune two resonators with stiffness mismatches smaller than ε_{lock}. This is more easily achieved when the two resonators are fabricated in close proximity, as shown in section III.B.

Note that making the first choice (3) together with $\gamma << 1$ leads to a higher sensitivity than (7), but to a reduction of the locking range (the former is inversely proportional to γ, and the latter is proportional to γ). Furthermore, the resolution is not improved, and the practical implementation of accurate electronic gains, as opposed to elementary digital blocks, is also an issue.

As for the MEMS resonators, several solutions exist as well (capacitive, piezoelectric, piezoresistive). The challenge is to have an output voltage in phase with the position of the resonator inside its gap without requiring any analog filters to match the theoretical optimal point. As described in [21], capacitive MEMS co-integrated with a capacitive readout (i.e. amplifier that integrates and amplifies the output current of the capacitive MEMS) appears to be the best solution to match the phase requirements and have enough voltage output to trigger the rest of the circuitry. Moreover, a stiffness mismatch can be obtained through the electrostatic softening phenomenon to have an easy way to measure the sensitivity to mismatch, as a proof of concept. The MILO must integrate two capacitive

flexural MEMS resonators with their readout, and the mixer described in Figure 3. The next part describes the design of this integration. This architecture also benefits from the fact that the duty cycle of V_{f1} and V_{f2} is proportional to the phase difference between them, and thus to the phase difference between the two MEMS resonators, giving an easy way to measure it. In this architecture, $\gamma = 1$.

III. Co-integration of a CMOS-MEMS MILO

A. About co-integration

To match the optimal performances of the MILO, the MEMS resonators must be nominally as close as possible in term of quality factor, mechanical stiffness, and natural frequency. Moreover, they must endure the same environmental drifts. This way these drifts have the same effect on the natural frequency of both resonators and leave the phase difference unchanged. Taking account of the CMOS fabrication process variability, it means that both resonators must be fabricated on the same chip, with their amplifier. We choose to fabricate the mixer on the same chip as well, to reduce the connections' length and prove its feasibility as a VLSI system, but it comes at the cost of high frequency perturbation. This choice is discussed in section ***. An equivalent architecture has already been tested [22] with separated blocks (i.e. one PCB for each resonator, and one PCB for the mixer) with limitations due to the intrinsic mismatch of the resonators. Moreover, the physical distance between the resonators disables a proper drift rejection. Co-integration shrinks the electrical consumption to the minimum and is much more predictable than having various PCBs in term of parasitic capacitances, delay in the connections between them. It comes at the cost of some level of complexity and unwanted coupling through the substrate and the connections. These issues are explained in section III.E. We now describe each of the co-integrated blocks, and compare simulation and experimental results. A complete CMOS-MEMS MILO schematic is given in Figure 11, and can be referred to throughout this section.

B. CMOS-MEMS resonators

The CMOS-MEMS resonators used in this work are composed of two parts, the resonator and its readout. In our case the resonators are fabricated in tungsten, which is the VIA layer in the AMS C35c4b3 process. Two CMOS-MEMS resonators are fabricated on each chip. The tungsten's Young modulus and density are respectively 411GPa at 25°C, 19300kg.m^{-3}. The geometry defined in the layout is a clamped-clamped beam of length: 30µm, width: 500nm, thickness: 900nm, actuation gap: 450nm. The structure is released from the silicon oxide with a 10 minutes wet etching in a bath of dissolved hydrofluoric oxide. The chip is then washed in distilled water for 10 minutes, followed by an 8 minutes bath of isopropyl alcohol to eliminate the water. Finally, it is heated for 10 minutes at 100°C to evaporate the remaining alcohol. The resonator is put in a three-port configuration (i.e. one electrode for the actuation and one for the output current). A schematic of such a configuration is given in Figure 4. The resonator is characterized by SEM imaging (see Figure 5). The gap is measured at 374nm instead of the 450nm specified in the layout, which is not unexpected given the fact that AMS is not a technology made for MEMS fabrication, and defining such VIA structures violates the design rules. The measured natural frequency at a bias voltage of 20V of both resonators of every sample fabricated in the run is given in Figure 6, with a mean value of 3.901MHz. This means that the tensile axial stress σ coming from the fabrication process can be estimated to be 488MPa. In Table 1 we sum up the important characteristics coming from this characterization

L (µm)	h (µm)	b (µm)	G_0 (µm)	Q	σ (MPa)
29.7	0.9	0.49	0.376	140	488

Table 1 Dimensions (length, height, thickness, all in micrometers) and characteristics of the clamped-clamped geometry of the MEMS resonators.

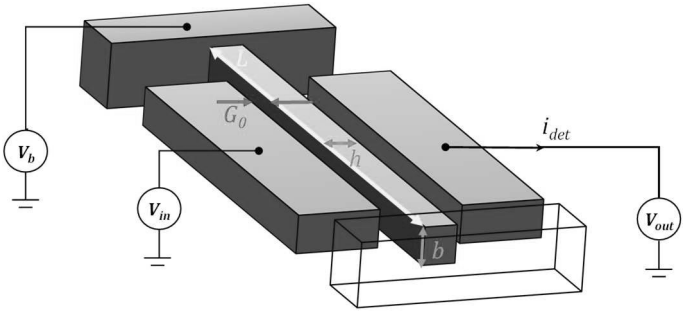

Figure 4: Schematic view of a clamped-clamped beam with a three-port configuration.

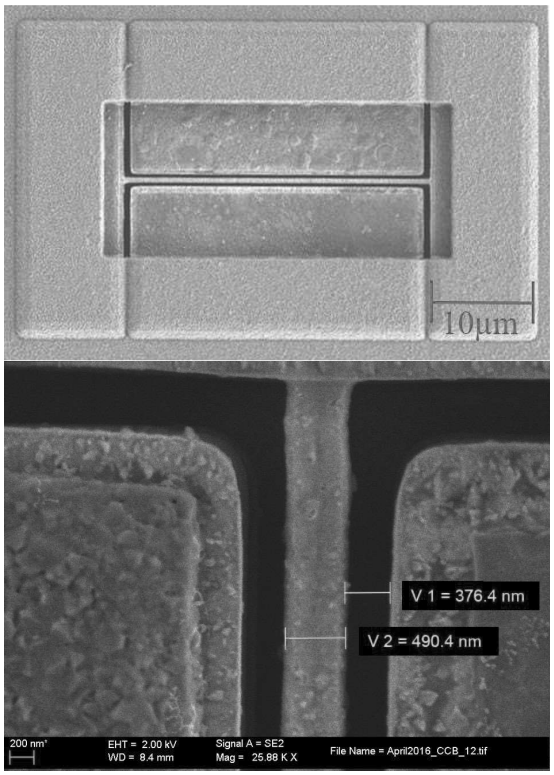

Figure 5: up: SEM image of the clamped-clamped beam. Bottom: zoom close to the anchor, with measured dimensions.

In order to perform simulations with the circuitry and taking into account the MEMS behaviour, a RLC model is developed and the values of the different electrical component

corresponding to such a geometry structures are obtained using the Euler-Bernoulli equation and a limited development [29].

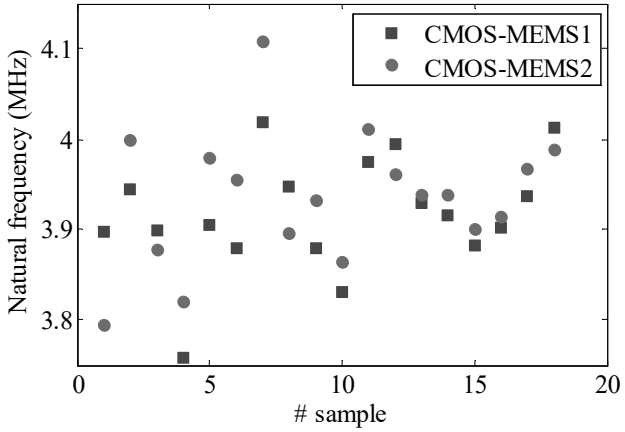

Figure 6: Natural frequency of the MEMS (at 20V of bias voltage) of various samples from the run.

We suppose that the resonator is in its linear regime, the quality factor is high (i.e. $Q>>1$), the bias voltage is high compared to the actuation one and that the resonators work in the linear regime, close to their resonance frequency. The extracted R_m, L_m and C_m values are presented Table 2, with ε_0 the vacuum permittivity, V_b the biasing voltage in Volts of the MEMS, Q the quality factor, E the Young's modulus in GPa, ρ the density in kg.m^{-3} and the dimensions defined in Figure 4, with the values corresponding to our geometry.

Component	Model	Value
R_m	$\frac{1.43hG^4}{L^2\varepsilon_0 b V_b^2}\sqrt{12.29\sigma\rho+\frac{41.7Eh^2\rho}{L^2}}$	31.88MΩ
L_m	$\frac{0.9\rho hG^4}{\varepsilon_0 tLV_b^2}$	178.6H
C_m	$\frac{\frac{\varepsilon_0 tLV_b^2}{0.9hG^4}}{\frac{41.71Eh^2}{L}+12.29\sigma L-\frac{3.2\varepsilon_0}{hG^3}V_b^2}$	9.32aF

Table 2 Values for the RLC model according to Juillard's model [29], and numerical applications corresponding to our clamped-clamped beam.

In our case, the motional resistance is of the order of 30MΩ at 25V of polarization, which means that the output current needs to be amplified by a transimpedance gain of the same order of magnitude to be exploitable. Moreover, one of the features of the capacitive MEMS resonators is that the output current is on phase with the velocity of the structure. Or as mentioned in section II, an output voltage on phase with the position is required to match with the theory developed in [21], which means having a phase close to 90° in the readout. Capacitive sensing architectures proposed by Verd [30] or Sobreviela [31] gives such a phase with appropriate gain. The amplifier used in this work is presented in [30]. The output current of the MEMS is integrated in the parasitic capacitances of the output electrode and the input transistor, providing the appropriate phase shift. It is then amplified by a differential cascode structure and followed by a source-follower output stage which acts as a 50Ω buffer (see [30] for further details). A post-layout (i.e. extracted) simulation of the Bode diagram of this amplifier is given in Figure 8. At 4MHz, the gain is at 29.4MΩ which compensate for the motional resistance of the resonator. And the phase is at 65°, but as it is mentioned in section III.C, the amplifier is followed by a digital mixer which adds a phase delay to reach the required 90° phase in the complete circuitry. The amplifier also benefits from a differential architecture that disables the effect of the feedthrough capacitance, by having a secondary unbiased resonator (the dummy MEMS, see Figure 7 for a microscopic image of a complete CMOS-MEMS device) at the non-inverter input of the differential pair. The input and output nodes are auto-biased. The frequency response of this CMOS-MEMS resonator is measured experimentally, and the RLC model plus the post-layout extracted model of the amplifier, taking into account all parasitic capacitances is simulated. The result is shown Figure 9, exhibiting an excellent agreement in term of gain and phase. The feedthrough is effectively cancelled.

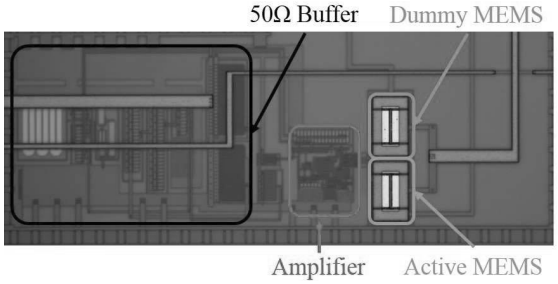

Figure 7 : microscopic view of a CMOS-MEMS resonator.

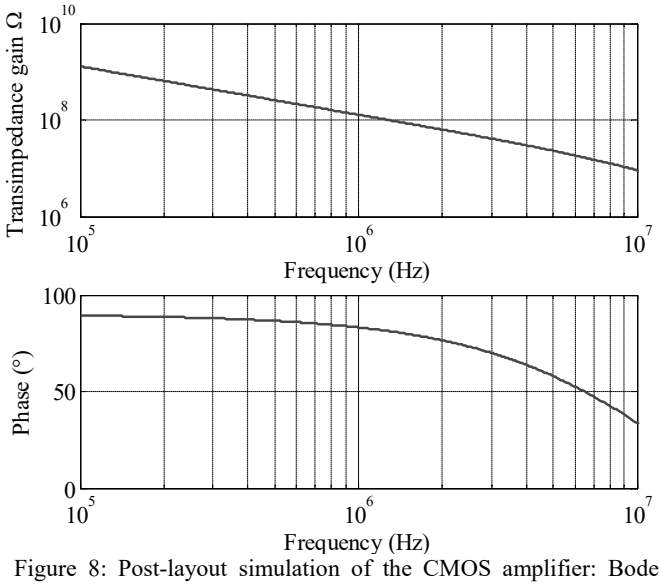

Figure 8: Post-layout simulation of the CMOS amplifier: Bode diagram.

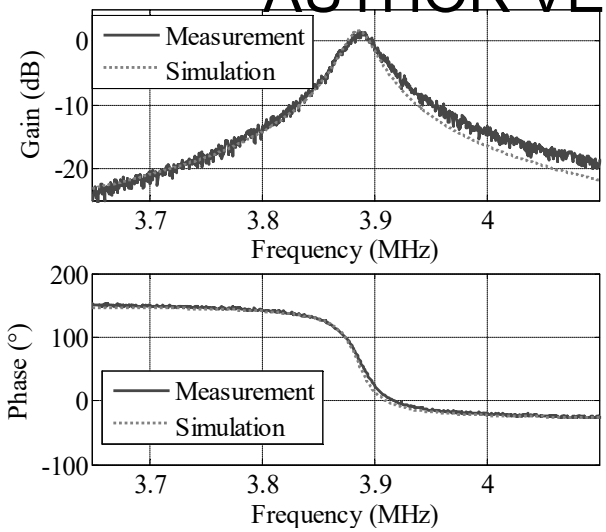

Figure 9: Experimental spectrum and post layout simulation of a tungsten cantilever beam (dimensions 30µm, 900nm, 485nm, Q=140, Gap=370nm), polarized at 25V.

C. Design of the digital mixer

As shown in Figure 2, the mixer is composed of two comparators, and three logical gates. The components we used are the one proposed in AMS 0.35 A_CELLS and CORELIBD libraries. The comparators have a 17mV hysteresis and 7ns delay, corresponding to a 10.9° phase delay at 4MHz. The architecture is a differential pair followed by a three inverter gates output stage for the saturation. A bias tee is added at the input of both comparators to ensure the stability of the triggering level, since the auto-bias of the output node of the amplifier changes with the amplitude of the output signal. This scheme is illustrated in Figure 11. The bias tee is composed of a 1MΩ resistance and 5pF capacitance. It induces no phase delay but a 2dB gain loss.

The logical gates' phase delay is around 0.3ns each because we chose the smallest one available in the CORELIBD library. This choice imposes, however, to add a digital buffer in order to output enough current to load the rest of the circuitry and the eventual oscilloscope probes. We designed a buffer composed of four stages of larger and larger inverter gates using AMS 0.35 CORELIBD NOT gates in parallel. The buffer enables low rise and fall times for charges up to 50pF but it generates high frequency noise due to its high AC current consumption. This issue will be discussed on the next paragraph. The buffer has a 1.2ns delay, corresponding to a 1.8° phase shift. The entire mixer leads to an 11.7° phase shift at 4MHz.

D. Excitation level adaptation

The mixer outputs 3.3V signals which is too much for the MEMS to remain inside its linear regime. Indeed, as it is shown in Figure 10, 1V of excitation amplitude is the maximum value for the resonator to keep its linear behaviour. A voltage divider bridge made of two potentiometer, one for each side is placed between the mixer's output and the resonators' input (see Figure 11). Since the bridge is placed outside the chip, it must be connected using wire bondings and SMA connectors, which adds more parasitic capacitances to load. Two options are considered, 10cm SMA wires, or 1cm SMA connectors which respectively are 8pF and 1pF load.

The 1kΩ potentiometers bridge has its own 8pF parasitic capacitance, generating an RC filter with a cutting frequency at 19MHz, which slightly filters the mixer's digital signal and adds a 5° phase at 4MHz.

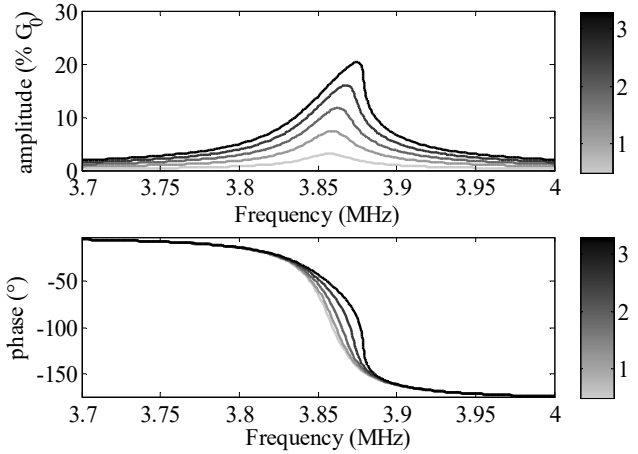

Figure 10: Amplitude of motion and phase response of the resonator for different excitation voltage.

E. Design of decoupling capacitances

The digital buffer induces an important AC current consumption which leads to supply voltage overshoots and drops. Decoupling capacitances composed of 10µm*10µm NMOS transistors with source and drain connected to the ground and gate to the supply voltage are placed all over the chip as a matrix. They are towered by 3 layers of metal alternately connected to the ground and the supply voltage in order to reduce the power supply access resistance and reduce the voltage drop effect. Moreover, they polarize the substrate at the ground which lowers the unavoidable electrical coupling between the resonators. The total distributed capacitance is 40pF, meaning that, by the standard "rule of thumb", the system is able to load up to 4pF without major perturbation. In Figure 12, both loads (8pF and 1pF) are put at the output of the mixer, showing the fact that the 8pF disturbs heavily the system, generating DC drops and overshoots which affect the amplifiers.

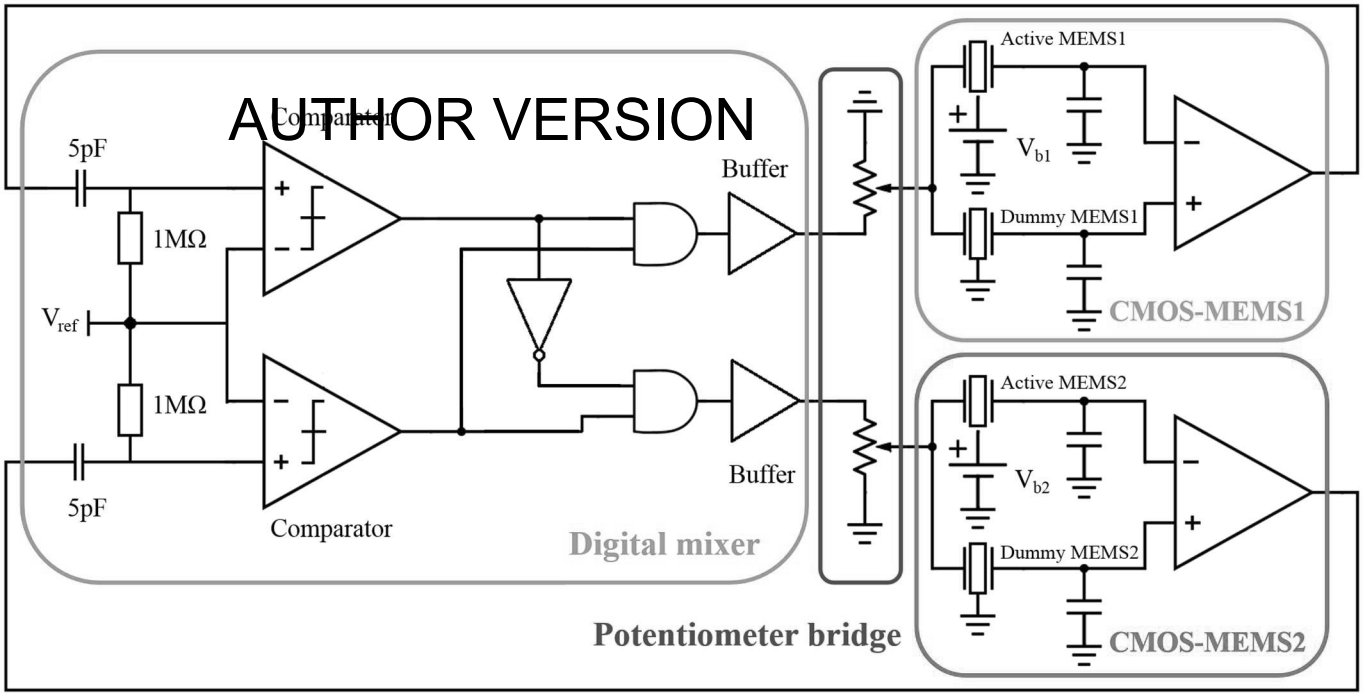

Figure 11: Schematic of the entire CMOS-MEMS MILO architecture used in this work. Only the potentiometer bridge is not co-integrated.

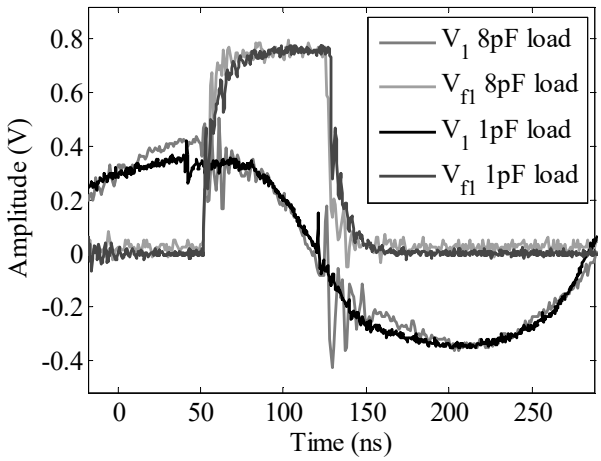

Figure 12: Open loop oscillogram of one side of the MILO with 10cm SMA wire between the mixer and the bridge (8pF load) or 1cm SMA connector (1pF load).

F. Chip's final organization and layout

The Figure 13 shows a microscopic view of the fully co-integrated CMOS-MEMS MILO. The critical connections have to be the smallest ones, i.e. between the resonator and the amplifier, or the amplifier and the comparator, because they are analog connections, susceptible to noise interferences. The organization had to be in straight line to enable the use of a HTT Wedge7 probe card. Three pads are routed to the ground to properly evacuate parasitic currents from the substrate. We make sure that two AC signals are not routed to neighbour PADs to avoid parasitic coupling. This organization comes at the cost of having a very long (1mm) connection between the comparators' output and mixer's inputs, since the comparators are at each extremity of the chip and the mixer at the centre. These connections are fabricated using the top metal layer to lower the parasitic capacitance with the substrate, but remain the weaker link. Moreover, due to the post-process HF wet etching, the top layer is always slightly etched as well, even under the Si_3N_4 protection layers. This leads to an increase of the local volumetric current, heating and possibly a rupture in the connection.

IV. Experimental results

The experimental flow is as follows. After the wet etching, a first electrical measurement is made using the HTT Wedge7 probe card and a probe station, to ensure the proper release of the structures. The probe card enables quick and easy measurements on the CMOS-MEMS resonators, however, it adds too much parasitic capacitance between the lines to be suited for further measurements. If the liberation occurred properly, the chip is placed on a golden PCB and wire-bonded, which disables the capacitive coupling between the lines. Then the resonators are fully characterized, and the MILO is measured step by step: open loop, close loop, common mode rejection and sensitivity to mismatch, short term stability and long term stability. This section describes these steps, but first we mention the benefits from co-integration, recalling the hypothesis made in section III.A.

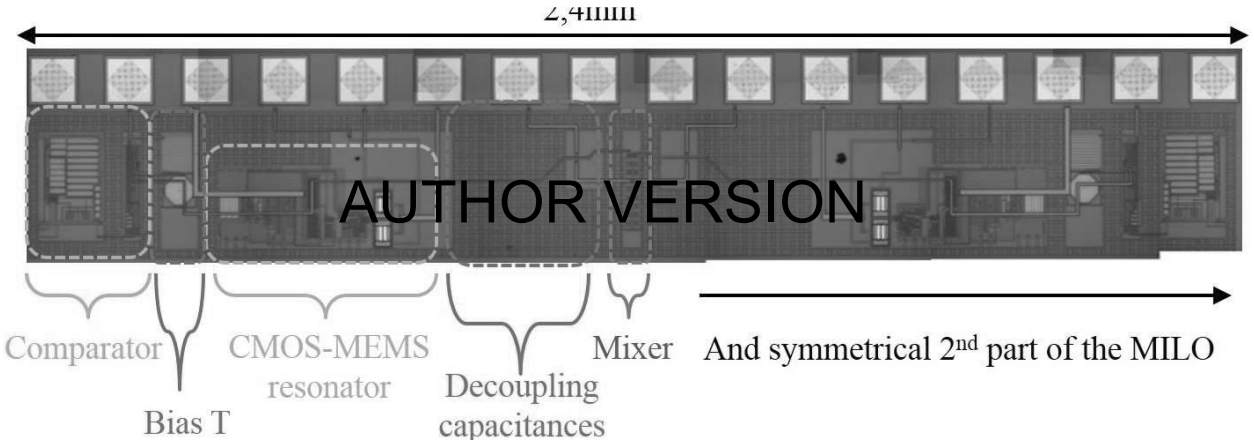

Figure 13: microscopic image of the chip showing each block of the fully co-integrated CMOS-MEMS MILO

A. *Benefits from co-integration*

Co-integration is required, in our case, for several reasons. First, to ensure the fact that both resonators endure the same environmental drifts, by fabricating them as close as possible. Second, to lower the intrinsic mismatches coming from the fabrication process, especially concerning the natural frequency. And third, because in a VLSI perspective, co-integration lowers the area and power consumption of the device. As mentioned in section III.B, Figure 6 shows the natural frequency of two CMOS-MEMS resonators for various samples fabricated in the run. The standard deviation on the frequency difference between one resonator and every other one is 55kHz, while it is 23kHz for the frequency difference only between co-integrated resonators. It means co-integrating two resonators lowers the natural frequency mismatch coming from the fabrication process by a factor 2.4, with the possibility to find very well matched resonators (i.e. less than 10 kHz of natural frequency mismatch). Moreover, the static consumption is 30mW compared to the 125mW of the non-co-integrated version of [23].

B. *Open loop characterization*

This characterization is performed to achieve two goals. First, to obtain the resonators' spectra for different biasing voltages, extract the matching conditions, and then to obtain the experimental phase delays of the MILO, since they heavily influence its performance. The spectra are obtained using an Agilent E5100A Network analyser, results are shown Figure 14. The extracted quality factors are 120 for MEMS1 and 140 for MEMS2. They are matched as long as MEMS1 bias voltage is around 2V lower than MEMS2's. The gain mismatch, due to a mismatch in the gap distance, is without consequence since the amplifiers load comparators and only the zero-crossings are important. They are then excited using a Tektronix AFG3052C waveform generator at the resonance frequency. This generator outputs two signals (V_{exc1} and V_{exc2}) with controllable phase shift, which is set at 90°. The excitation sinusoid, amplifiers' output and mixer's output are recorded on a Tektronix MSO5024B oscilloscope. We plot the MILO's open loop in Figure 15. There is a 8.3° phase shift between the excitations signals and the mixer's outputs, due to the fact that the 65° phase shift in the amplifier, plus the 11.7° in the mixer, and the 5° in the potentiometer bridge don't reach the optimal 90°, but 81.7 °. This is taken into account in the theoretical predictions.

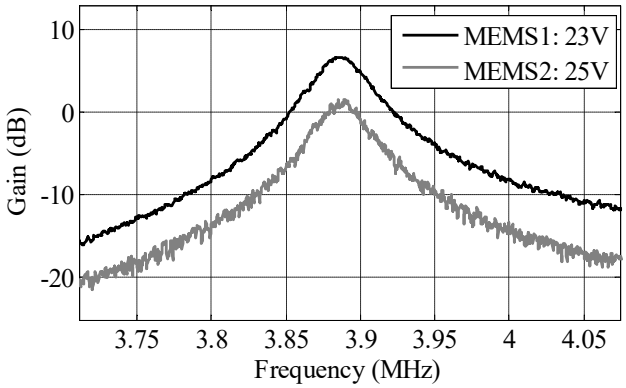

Figure 14: Spectra of the two CMOS-MEMS resonators. MEMS1 is biased at 23V, MEMS2 at 25V to achieve the frequency matching.

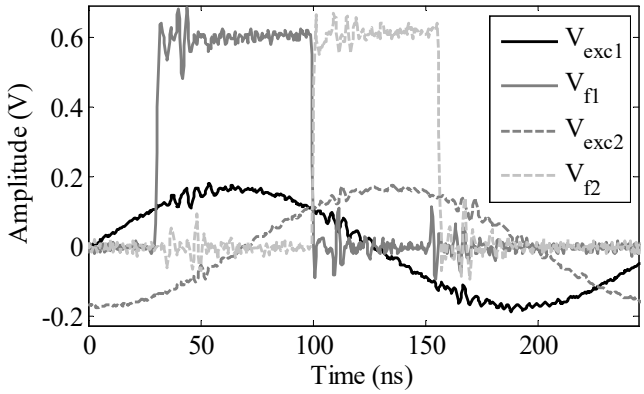

Figure 15: open loop oscillogram of the MILO.

C. *Closed-loop characterization: sensitivity to mismatch and drift rejection*

The loop is closed using the configuration depicted in Figure 16, and a closed loop oscillogram is given in Figure 17. The amplifiers are slightly saturated but it does not affect the MILO's behaviour since only zero-crossings are important.

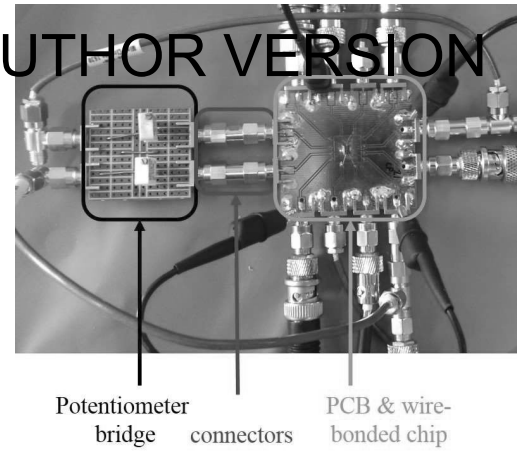

Figure 16: experimental set-up

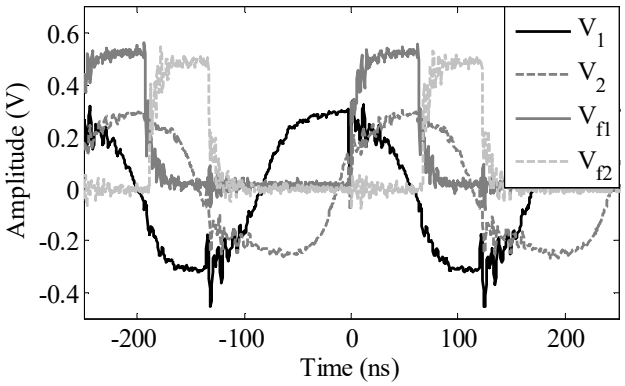

Figure 17: close loop oscillogram of the MILO, with respective biasing voltage of 20V and 22.3V for MEMS1 and MEMS2.

To investigate the MILO's sensitivity to the differential mode, we operate at the equilibrium point of respectively 35V and 37.3V for the bias voltage of MEMS1 and MEMS2. We then apply a relative electrostatic stiffness mismatch by tuning the bias voltage of MEMS2 while leaving the bias of MEMS1 fixed. The duty cycle of V_{f1} and V_{f2} changes, as well as the MILO's frequency, as represented in Figure 18. To determine the correspondence between the change of bias voltage δV and the relative stiffness mismatch ε, we use the fact that the model predicts a dependence of the MILO's frequency with respect to the stiffness mismatch of 1/4, independently of the parameters (quality factors, parasitic delays…) [21]. Given the -5.56kHz/V electrostatic softening, we infer the empirical formula:

$$\varepsilon \approx 5.9.10^{-3}\delta V \,. \qquad (4)$$

This enables the comparison between the experimental results to the theoretical predictions in term of sensitivity of the differential mode (i.e. relative stiffness mismatch). The results are plotted in Figure 19, showing a good matching between the theory and the experimental results. The experimental locking range is, though, a bit smaller than predicted ($|\varepsilon| < 8.88\times10^{-3}$ instead of $|\varepsilon| < 1.01\times10^{-2}$). This is an expected consequence of the non-idealities of the mixer when one of the pulse width gets close to 0. For this architecture, the phase difference is obtained from the duty cycles of V_{f1} and V_{f2} (named *DC1* and *DC2* through the formula:

$$\varphi = 90(1+\frac{DC1-DC2}{DC1+DC2}) \qquad (4)$$

The calculated phase difference variation is in agreement with the theory, given the quality factors of the MEMS and the 8.3° missing phase delay to reach the optimal phase condition, as mentioned in section IV.B. Finally, we plot the fractional phase difference versus the fractional frequency variation, for the experimental data and the theory. As expected, the locking range is smaller. The sensitivity enhancement (i.e. the slope of this curve) is 287.2. We plot in this graph as well the optimal case defined in section II (i.e. phase delays of exactly 90° in the readouts and 45° in the mixer, same quality factor). The sensitivity in the optimal case is 16.5% higher than in our case.

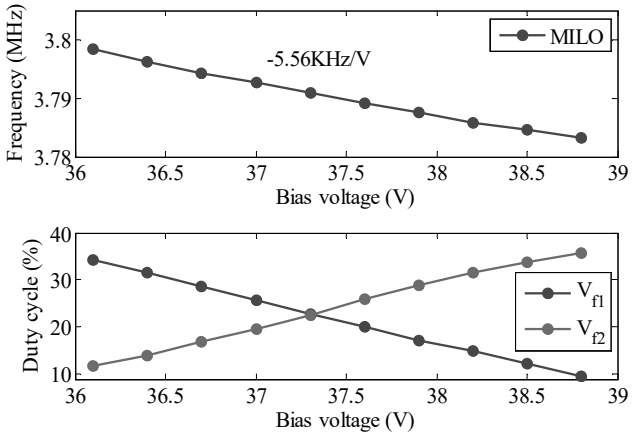

Figure 18: Frequency and Duty Cycle for the MILO for different values of the bias voltage of MEMS2.

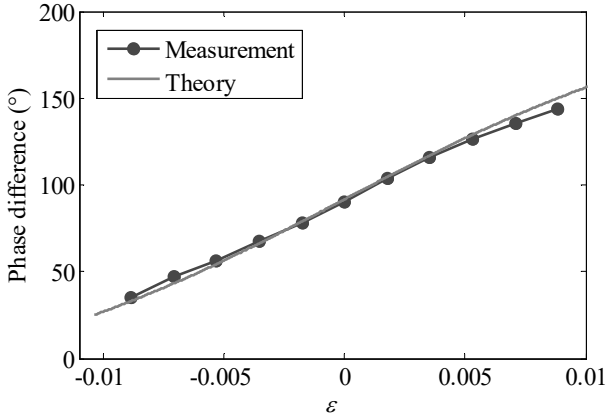

Figure 19 Experimental results and theoretical predictions (from [21]) of the phase difference variation with respect to the relative stiffness mismatch between the resonators.

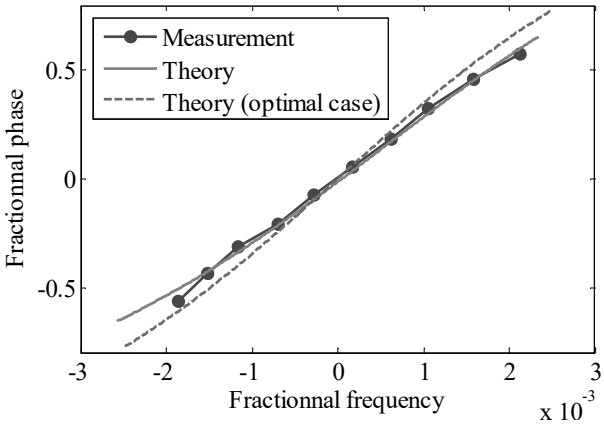

Figure 20: measurement of the fractional frequency versus the fractional phase and theoretical predictions from [21] in our case and in the optimal case

To investigate the MILO's ability to reject the environmental drifts (i.e. variation of physical parameters equally affecting both resonators, like temperature, humidity, pressure), the chip is placed over a thermal chuck. The MILO is started at the same equilibrium point (35V and 37.3V). The temperature is increased by 10°C steps up to 100°C, and the frequency, duty cycles of V_{f1} and V_{f2} are recorded, and plotted in Figure 21. The mechanical softening, induced by a lowering of the Young's modulus and the compensation of the tensile axial stress σ due to the tungsten's expansion when the temperature increases is at -1745Hz/°C. Even though the duty cycle remains stable, there is a slight drift when the chip reaches high temperature. This might be caused by a change of behavior of the amplifier, especially its phase, when the temperature is high. To investigate this point, we perform simulations on the post-layout extracted model of the MILO, changing the temperature on the Spectre simulator. We plot the fractional phase variation versus the fractional frequency for both common mode (i.e. environmental variations) and differential mode (i.e. relative stiffness variation induced by the tuning of MEMS2's bias voltage) in Figure 22, with the theory and the simulations. The drift in phase observed in the common mode is partially explained by the amplifier's behavior's drift with the temperature.

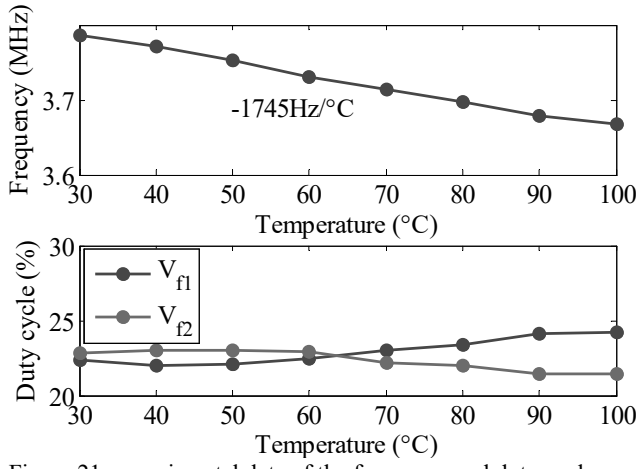

Figure 21: experimental data of the frequency and duty cycles over a 70°C temperature range.

The common mode is well rejected compared to the sensitivity of the fractional phase to the relative mismatch variation (ratio of 205). This section has described the common mode rejection capabilities and sensitivity to a relative stiffness mismatch between the two resonators of the MILO. A good agreement with the theory has been found.

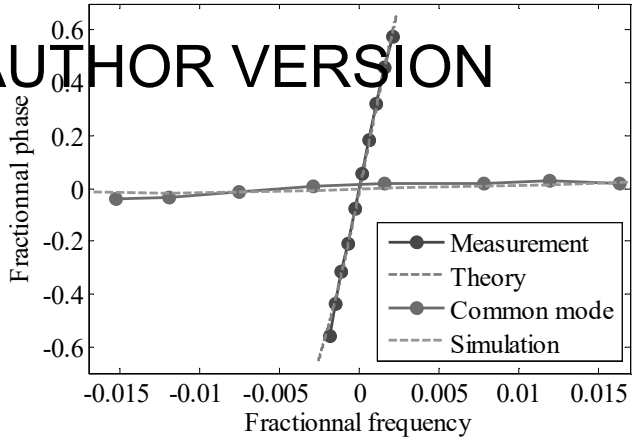

Figure 22: fractional phase VS fractional frequency for both differential mode and common mode, with theoretical results and post-layout simulation results.

V. Conclusion

In this article, we presented the monolithic co-integration of the MILO, the theoretical framework of which had been developed in our previous work [21]. Previous implementation, non-co-integrated, had already been presented [23], [20] with several issues coming from the intrinsic mismatch between the resonators and their distance, disabling a proper common mode rejection. By taking care of every aspect of the architecture, whether it is the electronic design of the chip (analog readout, digital mixer, decoupling capacitances, and connections), the experimental set-up (SMA wiring, capacitive loads), we obtain a very good agreement with the theoretical predictions in term of sensitivity of the phase difference to a relative stiffness mismatch. We proved the benefits of monolithic co-integration for the common-mode rejection capabilities of a MILO for two reasons: the reduction of the intrinsic mismatch between the resonators due to the fabrication process, and the closeness of the resonators to ensure the fact that they endure the same environmental drifts. We also proved the benefits of co-integration in term of power and area consumption compared to the non-co-integrated version. We finally proved experimentally the fact this architecture do not increase the resolution of the differential sensor since the gain in sensitivity is compensated by a loss in noise figure.

The architecture can still be optimized, through the design of an amplifier thermally stable and the co-integration of the voltage divider bridge for instance. Exploring the synchronization of two non-linear MEMS resonators, building a second feedback loop to ensure the fact that both resonators are kept at the quadrature, or conceiving the monolithic co-integration of other architectures (for $\gamma \neq 1$) are several leads to be followed to continue the exploration of the capabilities of synchronized MEMS oscillators for differential measurement applications.

[1] P. Hauptmann, "Resonant Sensors and Applications," *Sensors and Actuators A,* pp. 371-377, 1991.

[2] L. Khine, M. Palaniapan and W. K. Wong, "6Mhz Bulk-Mode Resonator with Q Values Exceeding One Million," *TRANSDUCERS 2007 - 2007 International Solid-State Sensors, Actuators and Microsystems Conference,* pp. 2445-2448, 2007.

[3] K. A. A. Makinwa, "Smart temperature sensors in standard CMOS," *Procedia Engineering,* vol. 5, pp. 930-939, 2010.

[4] SiTime, "Elite DualMEMS Architecture," [Online]. Available: https://www.sitime.com/technology/mems-oscillators/architecture/elite-dualmems.

[5] H. Lee, A. Partridge and F. Assaderaghi, "Low jitter and temperature stable MEMS oscillators," *2012 IEEE International Frequency Control Symposium Proceedings,* pp. 1-5, 2012.

[6] A. A. Trusov, S. A. Zotov, B. R. Simon and A. M. Shkel, "Silicon accelerometer with differential Frequency Modulation and continuous self-calibration," *2013 IEEE 26th International Conference on Micro Electro Mechanical Systems (MEMS),* pp. 29-32, 2013.

[7] A. Norouzpour-Shirazi et al., "A dual-mode gyroscope architecture with in-run mode-matching capability and inherent bias cancellation," *2015 Transducers - 2015 18th International Conference on Solid-State Sensors, Actuators and Microsystems (TRANSDUCERS),* pp. 23-26, 2015.

[8] J. C. Salvia et al., "Real-Time Temperature Compensation of MEMS Oscillators Using an Integrated Micro-Oven and a Phase-Locked Loop," *Journal of Microelectromechanical Systems,* vol. 19, no. 1, pp. 192-201, 2010.

[9] Y. Chen, D. D. Shin, I. B. Flader and T. W. Kenny, "Tri-mode operation of highly doped silicon resonators for temperature compensated timing references," *IEEE 30th International Conference on Micro Electro Mechanical Systems (MEMS),* pp. 1158-1161, 2017.

[10] Y. Chen et al., "Ovenized dual-mode clock (ODMC) based on highly doped single crystal silicon resonators," *2016 IEEE 29th International Conference on Micro Electro Mechanical Systems (MEMS),* pp. 91-94, 2016.

[11] P. Thiruvenkatanathan, J. Yan and A. A. Seshia, "Differential Amplification of Structural Perturbations in weakly Coupled MEMS Resonators," *IEEE Transactios on Ultrasonics, Ferroelectrics and Frequency Control,* vol. 57, no. 3, pp. 690-697, 2010.

[12] C. Zhao et al., "A review on coupled MEMS resonators for sensing applications utilizing mode localization," *Sensors and Actuators A: Physical,* vol. 249, pp. 93-111, 2016.

[13] M. Spletzer, A. Raman, A. Q. Wu and X. Xu, "Ultrasensitive mass sensing using mode localization in coupled microcantilevers," *Applied Physics Letters,* vol. 88, p. 254102, 2006.

[14] C. Zhao, G. S. Wood, J. Xie, H. Chang, S. H. Pu and M. Kraft, "A Three Degree-of-Freedom Wealky Coupled Resonator Sensor With Enhanced Stiffness Sensitivity," *Journal of Microelectromechanical Systems,* vol. 25, no. 1, pp. 38-51, 2016.

[15] C. Zhao et al., "A Comparative Study of Output Metrics for a MEMS Resonant Sensor Consisting of Three Weakly Coupled Resonators," *Journal of Microelectromechanical Systems,* vol. 25, no. 4, pp. 626-636, 2016.

[16] P. Thiruvenkatanathan, J. Yan, J. Woodhouse and A. A. Seshia, "Enhancing Parametric Sensitivity in Electrically Coupled MEMS Resonators," *Journal of Microelectromechanical Systems,* vol. 18, no. 5, pp. 1077-1086, 2009.

[17] J. Juillard, P. Prache, P. Maris Ferreira and N. Barniol, "Impact of output metric on the resolution of mode-localized MEMS resonant sensors," *2017 IEEE International Frequency Control Symposium (IFCS),* 2017.

[18] C. Zhao, G. S. Wood, S. H. Pu and M. Kraft, "A Feasibility Study for a Self-oscillating Loop for a Three Degree-of-Freedom Coupled MEMS Resonator Force Sensor," *Procedia Engineering,* vol. 120, pp. 887-891, 2015.

[19] C. Zhao, M. Pandit, B. Sun, G. Sobreviela, X. Zou and A. Seshia, "A Closed-Loop Readout Configuration for Mode-Localized Resonant MEMS Sensors," *Journal of Microelectromechanical Systems ,* vol. PP, pp. 1-3, 2017.

[20] J. Juillard, A. Bonnoit, N. Barniol, A. Uranga and G. Vidal-Alvarez, "A Novel Architecture for Differential Resonant Sensing," *Procedia Engineering,* vol. 87, pp. 1573-1576, 2014.

[21] J. Juillard, P. Prache and N. Barniol, "Analysis of Mutually Injection-Locked Oscillators for Differential Resonant Sensing," *IEEE Transactions on Circuits and Systems I: Regular Papers,* vol. 63, pp. 1055-1066, 2016.

[22] P. Prache, A. Uranga, N. Barniol and J. Juillard, "Temperature-drift rejection and sensitivity to mismatch of synchronized strongly-coupled M/NEMS resonators," *2016 IEEE 29th International Conference on Micro Electro Mechanical Systems (MEMS),* pp. 1054-1057, 2016.

[23] P. Prache, P. M. Ferreira, N. Barniol and J. Juillard, "Monolithic integration of mutually injection-locked CMOS-MEMS oscillators for differential resonant sensing applications," *2016 IEEE International Conference on Electronics, Circuits and Systems (ICECS),* pp. 756-759, 2016.

[24] R. Adler, "A Study of Locking Phenomena in Oscillators," *Proceedings of the I.R.E. and Waves and Electrons,* pp. 351-357, 1946.

[25] A. Mirzaei, M. E. Heidari, R. Bagheri, S. Chehrazi and A. A. Abibi, "The Quadrature LC Oscillator: A Complete Potrait Based on Injection Locking," *IEEE Journal of Solid-State Circuits,* vol. 42, no. 9, pp. 1916-1932, 2007.

[26] D. K. Agrawal, J. Woodhouse and A. A. Seshia, "Synchronisation in a coupled architecture of microelectromechanical oscillators," *Journal of Applied Physics,* p. 115, 2014.

[27] M. Matheny et al., "Phase Synchronization of Two Anharmonic Nanomechanical Oscillators," *Physical Review Letters,* p. 112, 2014.

[28] O. Shoshani and S. W. Shaw, "Phase Noise Reduction and Optimal Operating Conditions for a Paris of Synchronized Oscillators," *IEEE Transactions on Circuits and Systems,* vol. 63, no. 1, pp. 1-11, 2016.

[29] J. Juillard, G. Arndt and E. Colinet, "Modeling of Micromachined Beams Subject to Nonlinear Restoring or Damping Forces," *Journal of Microelectromechanical Systems,* vol. 20, no. 1, pp. 165-177, 2011.

[30] J. Verd, A. Uranga, J. Segura and N. Barniol, "A 3V CMOS-MEMS oscillator in 0.35µm CMOS technology," *2013 Transducers & Eurosensors XXVII: The 17th International Conference on Solid-State Sensors, Actuators and Microsystems,* pp. 806-809, 2013.

[31] G. Sobreviela, A. Uranga and N. Barniol, "Tunable transimpedance sustaining-amplifier for high impedance CMOS-MEMS resonators," *2014 10th Conference on Ph.D. Research in Microelectronics and Electronics (PRIME),* pp. 1-4, 2014.

[32] A. Bilotti, G. Montreal and R. Vig, "Monolithic magnetic Hall sensor using dynamic quadrature offset cancellation," *IEEE Journal of Solid-State Circuits,* vol. 32, pp. 829-836, 1997.

[33] G. K. Ho, K. Sundaresan, S. Pourkamali and F. Ayazi, "Temperature compensated IBAR reference oscillators," *19th IEEE International Conference on Micro ElectroMechanical Systems,* pp. 910-913, 2006.